

Stabilization of Tetragonal Phase and Aluminum-Doping Effect in a Bilayer Nickelate

Jia-Yi Lu^{1*†}, Yi-Qiang Lin^{1†}, Kai-Xin Ye^{2†}, Xin-Yu Zhao¹,
Jia-Xin Li¹, Ya-Nan Zhang², Hao Li³, Bai-Jiang Lv³,
Hui-Qiu Yuan^{2,4,5*}, Guang-Han Cao^{1,5,6*}

¹School of Physics, Zhejiang University, Hangzhou 310058, China.

²Center for Correlated Matter and School of Physics, Zhejiang University, Hangzhou 310058, China.

³Key Laboratory of Neutron Physics and Institute of Nuclear Physics and Chemistry, China Academy of Engineering Physics, Mianyang, 621999, China.

⁴Institute for Advanced Study in Physics, Zhejiang University, Hangzhou 310058, China.

⁵Institute of Fundamental and Transdisciplinary Research, and State Key Laboratory of Silicon and Advanced Semiconductor Materials, Zhejiang University, Hangzhou 310058, China.

⁶Collaborative Innovation Centre of Advanced Microstructures, Nanjing University, Nanjing, 210093, China.

*Corresponding author(s). E-mail(s): lujiayi0522@zju.edu.cn;
hqyuan@zju.edu.cn; ghcao@zju.edu.cn;

†These authors contributed equally to this work.

Abstract

Recent studies suggest that the tetragonal phase of the Ruddlesden-Popper (RP) bilayer nickelate, $\text{La}_3\text{Ni}_2\text{O}_7$ or $\text{La}_2\text{PrNi}_2\text{O}_7$, which is stabilized under high pressures, is responsible for high-temperature superconductivity (HTSC). In this context, realization of the tetragonal phase at ambient pressure could be a rational step to achieve the goal of ambient-pressure HTSC in the nickelate system.

By employing the concept of Goldschmidt tolerance factor, we succeed in stabilizing the tetragonal phase by aluminum doping together with post annealing under moderately high oxygen pressure. X-ray and neutron diffractions verify the tetragonal $I4/mmm$ structure for the post-annealed samples $\text{La}_3\text{Ni}_{2-x}\text{Al}_x\text{O}_{7-\delta}$ ($0.3 \leq x \leq 0.5$). The Al-doped samples, including the tetragonal ones, show semiconducting properties, carry localized magnetic moments, and exhibit spin-glass-like behaviors at low temperatures, all of which can be explained in terms of charge carrier localization. Furthermore, high-pressure resistance measurements on post-annealed samples reveal that even a low Al doping ($x = 0.05$) suppresses superconductivity almost completely. This work gives information about the effect of nonmagnetic impurity on metallicity as well as superconductivity in bilayer nickelates, which would contribute to understanding the superconducting mechanism in RP nickelates.

1 Introduction

The recent discovery of high- T_c superconductivity (HTSC) at about 80 K in the pressurized bilayer perovskite nickelate, $\text{La}_3\text{Ni}_2\text{O}_7$, represents a remarkable advance in the field of superconductivity research [1–3]. Unlike the infinite-layer nickelate superconductor discovered in 2019 [4], where the electronic configuration of nickel is nearly $3d^9$ (Ni^{1+}), the bilayer nickelate has an electronic configuration of $3d^{7.5}$ ($\text{Ni}^{2.5+}$). The apical oxygen site between the NiO_2 bilayers is almost fully occupied, in contrast with the absence of apical oxygen in the infinite-layer system. The oxygen occupancy not only greatly alters the Ni valence state, but also gives rise to strong interlayer coupling within the bilayers, the latter of which is widely accepted to be crucial for the emergence of HTSC [1, 5–14]. Currently, one of the major challenges in the research of nickelate superconductors is to realize bulk HTSC at ambient pressure, such that in-depth experimental investigations on the HTSC can be carried on. Note that while the pressure-quench protocol has successfully stabilized the high-pressure superconducting phase in $\text{Bi}_{0.5}\text{Sb}_{1.5}\text{Te}_3$ [15], this approach has not yet been replicated in nickelate superconductors [16].

The bilayer nickelate $\text{La}_3\text{Ni}_2\text{O}_7$ is an $n = 2$ member of the Ruddlesden-Popper (RP) series [17–21], $\text{La}_{n+1}\text{Ni}_n\text{O}_{3n+1}$, where n is the number of perovskite LaNiO_3 layers in between rocksalt-type LaO layers. At ambient pressure, the NiO_6 octahedra in $\text{La}_3\text{Ni}_2\text{O}_7$ are distorted and rotated, resulting in an orthorhombic structure with space group $Amam$ (No. 63) (this space group is based on a nonstandard setting, such that the c axis retains to be the longest one, consistent with the longest c axis in the tetragonal structure) [21]. Upon applying pressure, $\text{La}_3\text{Ni}_2\text{O}_7$ undergoes phase transitions to another orthorhombic structure ($Fmmm$, No. 69) [1] and further to a tetragonal structure (space group $I4/mmm$, No. 139) [22, 23]. Importantly, the out-of-plane Ni–O–Ni bond angle of those high-pressure stabilized structures turns out to be 180° , which effectively enhances the interlayer coupling. Moreover, a structural transition from $Amam$ directly to $I4/mmm$ at about 11 GPa was observed in $\text{La}_2\text{PrNi}_2\text{O}_7$ [24], concurrently with the emergence of superconductivity. A similar structural transformation into $I4/mmm$ tetragonal phase accompanying with appearance of bulk superconductivity is also observed in the trilayer nickelate $\text{La}_4\text{Ni}_3\text{O}_{10}$ [25],

which further corroborates the close relationship between crystal structure and HTSC. Very recently, it was found that compressively strained bilayer-nickelate thin films, which show superconductivity at ambient pressure [26–28], also adopt a tetragonal structure [27]. All the information above stimulates the research towards stabilization of the tetragonal structure, which at least serves as an initial step to ultimately realize ambient-pressure HTSC in *bulk samples* of the bilayer nickelate.

The concept of Goldschmidt tolerance factor [29], defined by $\tau = \frac{r_{\text{La}} + r_{\text{O}}}{\sqrt{2}(r_{\text{Ni}} + r_{\text{O}})}$, where τ refers to the ionic radii of the constituent ions, gives a clue to obtain the target tetragonal phase. In the view of crystal chemistry, the tolerance factor basically describes the stability as well as the tendency of lattice distortion in the perovskite-like block layers [30]. Using the effective ionic radii [31], and taking $r_{\text{Ni}^{2.5+}} = (r_{\text{Ni}^{2+}} + r_{\text{Ni}^{3+}})/2 = 0.625 \text{ \AA}$ for $\text{La}_3\text{Ni}_2\text{O}_7$, one obtains $\tau = 0.916$, suggesting that the perovskite-like layers are significantly compressed by the rocksalt LaO layers, which accounts for the orthorhombic distortion at ambient pressure. If the τ value increases towards 1.0 through suitable chemical substitutions, one expects that the tetragonal phase could be stabilized at ambient pressure. Indeed, a tetragonal bilayer RP phase in Sr-Ni-O system was realized through Al doping [32, 33], and via high-pressure synthesis [34], where the τ value is nearly 1.0. The theoretical calculations [35] suggest that the $Fmmm$ structure can be stabilized at ambient pressure by replacing the La^{3+} ion with a larger cation, either Ba^{2+} or Ac^{3+} . $\text{Ac}_3\text{Ni}_2\text{O}_7$ is also predicted to crystallize in the tetragonal $I4/mmm$ structure [36]. Unfortunately, the element Ac is almost unavailable because of its strong radioactivity and, on the other hand, the allowed solubility limit of Ba in $\text{La}_3\text{Ni}_2\text{O}_7$ is too small to increase the τ value appreciably [37, 38]. Considering the efficiency of Al doping in stabilizing La-Ni-O tri-layer structures [39] and its substantial doping capacity in related RP phases [32, 39], partial substitution of Ni sites with smaller cations Al^{3+} ($r_{\text{Al}^{3+}} = 0.535 \text{ \AA}$) might be a viable approach. Although the Al-doping definitely induces disorder, it still can serve as a probe to investigate the effect of nonmagnetic disorder on Anderson localization as well as potential superconductivity.

In this paper, we report our successful realization of the tetragonal phase in the bilayer nickelate $\text{La}_3\text{Ni}_{2-x}\text{Al}_x\text{O}_{7-\delta}$. Single-phase samples were obtained in the Al doping range of $0 \leq x \leq 0.5$. While all the as-prepared samples remain orthorhombic, the orthorhombicity tends to decrease with the Al doping. After post annealing under moderately high oxygen pressure, strikingly, the samples with $0.3 \leq x \leq 0.5$ finally become tetragonal. The detailed crystal structure of the typical samples of $x = 0.4$ was determined by X-ray and neutron powder diffractions. Transport and magnetic measurements under ambient pressure demonstrate that Al doping induces strong carrier localization. High-pressure resistance studies reveal a rapid suppression of superconductivity in $\text{La}_3\text{Ni}_{2-x}\text{Al}_x\text{O}_{7-\delta}$ ($x = 0.05, 0.1, \text{ and } 0.4$).

2 RESULTS AND DISCUSSION

Polycrystalline samples of $\text{La}_3\text{Ni}_{2-x}\text{Al}_x\text{O}_{7-\delta}$ ($x = 0, 0.05, 0.1, 0.2, 0.3, 0.4, 0.5, 0.6$) were prepared by solid-state reactions with using a sol-gel produced precursor [18, 24].

All the samples with $x \leq 0.5$ remain to be monophasic, as checked by powder X-ray diffractions (XRD), yet impurity phases appear for the sample of $x = 0.6$. This means that the Al solubility limit is about $x = 0.5$ under current synthesis conditions. The as-prepared monophasic samples were annealed at 500 °C under ~ 10 MPa oxygen atmosphere, the outcome of which is called post-annealed samples. Details of the sample preparation and treatment are provided in Methods. The chemical composition and homogeneity were checked by energy dispersive X-ray (EDX) spectroscopy. The results show homogeneous composition that is almost identical to the nominal stoichiometry within the measurement uncertainty for cations including the dopant Al [Figure S1 in the Supporting Information (SI)].

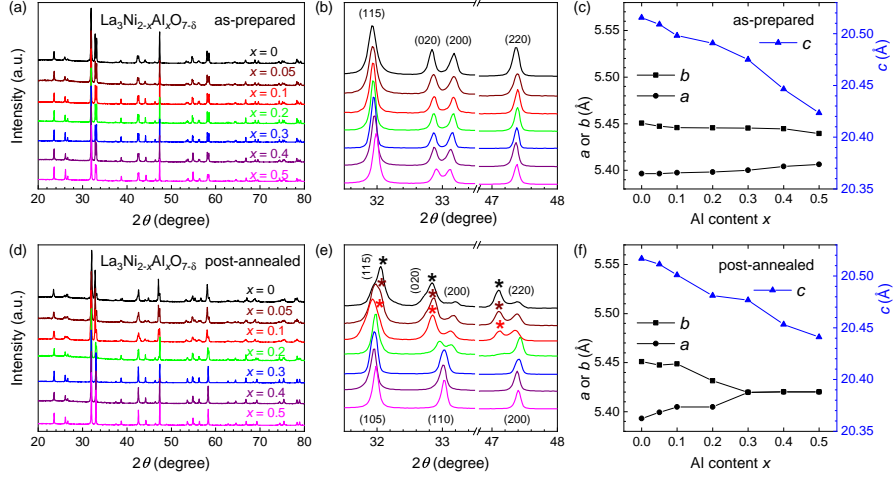


Fig. 1 Characterization of as-prepared (a-c) and post-annealed (d-f) samples of $\text{La}_3\text{Ni}_{2-x}\text{Al}_x\text{O}_{7-\delta}$ ($0 \leq x \leq 0.5$) by powder X-ray diffractions. In panel (e), the peaks marked by asterisks are attributed to a new phase formed during the annealing (see the text and SI). Plots (c) and (f) show lattice parameters as functions of Al content x . The error bars are smaller than the symbols.

Figures 1(a-c) show the XRD results for the as-prepared samples of $\text{La}_3\text{Ni}_{2-x}\text{Al}_x\text{O}_{7-\delta}$ ($0 \leq x \leq 0.5$). All the XRD peaks can be well indexed with the *Amam* structure [21], and no secondary phase is detectable. The lattice parameters are calculated by least-squares fit of the reflections indexed, which are plotted as functions of Al content x in Figure 1(c). One sees that the c axis is reduced significantly by the Al doping, which is attributed to the smaller size of Al^{3+} ions compared with $\text{Ni}^{2.5+}$ ions. Meanwhile, the a and b axes only change slightly, and they tend to get closer with the Al doping. The orthorhombicity, defined by $\epsilon = 2(b-a)/(b+a) \times 100\%$, decreases from 1.00% for $x = 0$ to 0.61% for $x = 0.5$, which aligns with the increase of the tolerance factor. Nevertheless, our aim for the tetragonal structure is not achieved yet in those as-prepared samples.

In order to obtain the target tetragonal phase, we tried to increase the oxygen content by annealing the samples under high oxygen pressure (see Methods for the details). The result is presented in Figures 1(d-f). For the non-doped sample of $x = 0$, first of

all, the intensity of (220) reflection at $2\theta \approx 47.4^\circ$ is obviously reduced [Figure 1(e)], and an additional peak nearby (marked with asterisks) appears, indicating formation of a new phase. A similar observation was also reported very recently [40]. The new phase (here we call it β phase) can be best fitted with a tetragonal $I4/mmm$ unit cell: $a = 3.8552(1) \text{ \AA}$ and $c = 20.2120(8) \text{ \AA}$, both of which are very close to those of the tetragonal $\text{La}_3\text{Ni}_2\text{O}_7$ phase reported very recently [41, 42]. The weight fraction of the β phase is 75.4%, as opposed to 24.6% for the remaining α phase. The α phase has the normal orthorhombic bilayer $Amam$ structure, with almost identical lattice parameters of the as-prepared sample (Figure S2 in SI). For the sample of $x = 0.1$, the two-phase Rietveld analysis yields similar lattice parameters for the α and β phases, yet shows a reversed result (80.5% and 19.5%, respectively) for their weight percentages. The fraction of new phase for $x = 0.2$ is near the XRD detection limit, say 1-5 wt.%, because only discernibly small signal from the new phase is seen.

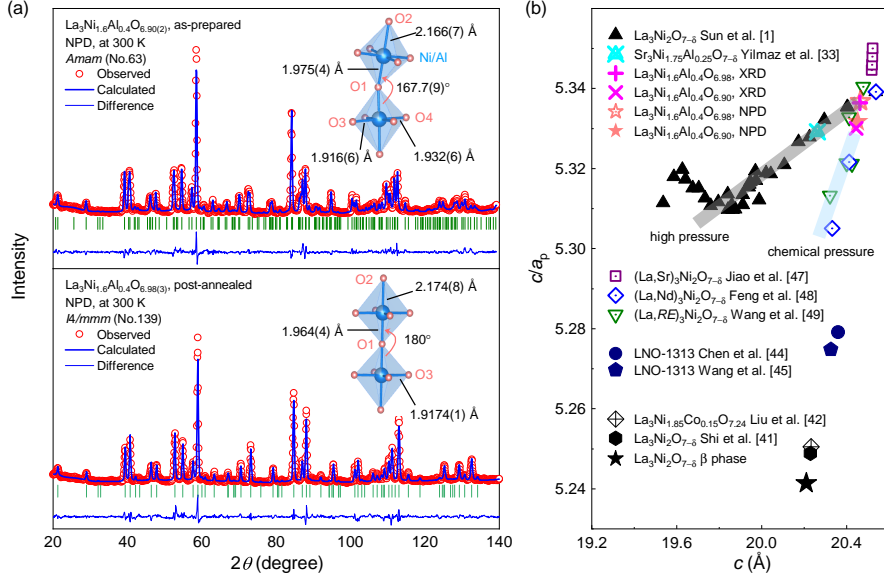


Fig. 2 (a) Rietveld refinement profiles of the neutron diffractions for the as-prepared (top) and post-annealed (bottom) samples of $\text{La}_3\text{Ni}_{1.6}\text{Al}_{0.4}\text{O}_{7-\delta}$. The insets show bond distances and angles in the NiO_6 bilayers. (b) The axial ratios c/a_p as functions of c for the bilayer and monolayer-trilayer (1313) nickelates. The simple perovskite unit, $a_p = \frac{1}{2}\sqrt{a^2 + b^2}$, is employed to effectively compare the tetragonal phases with orthorhombic ones.

For the heavily-doped samples of $0.3 \leq x \leq 0.5$, interestingly, the original (020) and (200) reflections (on the basis of an orthorhombic lattice) merge into a single peak [(110) reflection in the tetragonal lattice, Figure 1(e)], suggesting formation of the target tetragonal structure. Note that this tetragonal phase is different from the β phase mentioned above (see below). Figure 1(f) displays the lattice parameters as functions of Al doping, which clearly shows the structural evolution from orthorhombic

to tetragonal at $x \approx 0.3$. The result contrasts with that of the as-prepared samples [Figure 1(c)], underscoring the importance of annealing under high oxygen pressure.

To determine the oxygen stoichiometry, we performed thermogravimetric analysis (TGA) measurements on selected representative samples [shown in Figure S3 in SI]. The results demonstrate a clear enhancement in thermal stability with increasing Al doping concentration, as evidenced by reduced weight loss percentages [5.82% ($x = 0$) to 0.58% ($x = 0.4$) for as-prepared samples, 5.98% ($x = 0$) to 0.89% ($x = 0.4$) for post-annealed samples]. The result also shows that post-annealed samples consistently exhibit higher oxygen content than as-prepared counterparts. For $\text{La}_3\text{Ni}_{1.9}\text{Al}_{0.1}\text{O}_{7-\delta}$ samples, analysis of the weight-loss plateaus corresponding to $\text{La}_3\text{Ni}_{1.9}\text{Al}_{0.1}\text{O}_{6.45}$ [43] yields oxygen contents of about 6.87 (as-prepared) and 7.00 (post-annealed). The improved oxygen content and thermal stability in Al-doped systems suggest that Al incorporation may effectively stabilize the oxygen sublattice during thermal treatment.

The crystallographic data of the tetragonal phase were obtained by the Rietveld analysis based on the XRD slow-scan data. The XRD refinement profiles for the typical samples of $x = 0.4$ are displayed in Figure S3, and the resulted data are presented in Table S1, both of which are deposited in the SI. Note that the c -axis value of 20.4620(4) Å of the tetragonal sample of $x = 0.4$ is even obviously larger than that of the β phase of $x = 0$. It is also larger than that of the so-called 1313 phase (another polymorph of $\text{La}_3\text{Ni}_2\text{O}_7$, crystallizing in a hybrid monolayer-trilayer structure [44–46]). To highlight the differences, in Figure 2(b) we plot the axial ratios, c/a_p , where $a_p = \frac{1}{2}\sqrt{a^2 + b^2}$ in the case of an orthorhombic phase, as functions of c axis for various nominal “327” phases [44, 45, 47–49]. As is seen, the Al-doped tetragonal or orthorhombic phase has a similar axial ratio with those of the superconducting $\text{La}_3\text{Ni}_2\text{O}_7$ under high pressures [1], and with those of La-site doped $\text{La}_3\text{Ni}_2\text{O}_7$ [47–49]. However, the c/a_p value of the β phase is the smallest among the series. Thus the non-doped tetragonal β phase might possess substantially different structures which lead to absence of superconductivity even under high pressures [41].

To more precisely determine the oxygen positions and occupancies, we conducted neutron powder diffraction (NPD) measurements on both the as-prepared and the post-annealed samples of $x = 0.4$, as shown in Figure 2(a). The refined results, summarized in Table 1, reveal that the oxygen occupancies at the O1 site (*i.e.*, the apical site between NiO_2 planes) increases from 0.90(2) in the as-prepared to 0.98(3) in the post-annealed samples. Notably, refinement of the post-annealed sample using a model that includes interstitial oxygen (adopting the configuration observed in $\text{La}_2\text{NiO}_{4+\delta}$ where excess oxygen resides between LaO layers [50, 51]) yields a higher R_{wp} value (8.8 %), suggesting absence of interstitial oxygen here. As illustrated in the insets of Figure 2(a), the Ni–O1–Ni bond angle changes expectedly from $167.7(9)^\circ$ (in the Amm phase) to 180° (in the $I4/mmm$ phase), expectedly increasing the interlayer coupling. At the same time, the Ni–O3–Ni bond also becomes straight in the tetragonal phase, which enhances the hybridization between $\text{Ni-}3d_{x^2-y^2}$ and $\text{O-}2p_{x/y}$. Albeit with the Al doping, contrastingly, the Ni–O bond distances in the NiO_6 octahedra do not change significantly. Based on the bond distances, the bond valence sums (BVS) [52] calculated (without consideration of the Al doping) are 2.55 and 2.62, respectively, for the

Table 1 Crystallographic data of the as-prepared (orthorhombic phase) and post-annealed (tetragonal phase) $\text{La}_3\text{Ni}_{1.6}\text{Al}_{0.4}\text{O}_{7-\delta}$ from neutron powder diffractions.

orthorhombic phase		$\text{La}_3\text{Ni}_{1.6}\text{Al}_{0.4}\text{O}_{6.90}$				
space group		$Amam$ (No. 63)				
a (Å)		5.4055(1)				
b (Å)		5.4438(1)				
c (Å)		20.4515(5)				
R_{wp} (%)		6.18				
S		1.65				
atom	site	x	y	z	occ.	U_{iso}
La(1)	4c	0.25	0.240(2)	0.5	1.00	0.009(1)
La(2)	8g	0.25	0.243(2)	0.3191(1)	1.00	0.009(1)
Ni/Al	8g	0.25	0.247(2)	0.0960(2)	0.80/0.20	0.003(1)
O(1)	4c	0.25	0.208(2)	0	0.90(2)	0.002(3)
O(2)	8g	0.25	0.283(1)	0.2015(3)	1.00	0.010(1)
O(3)	8e	0.5	0	0.1049(3)	1.00	0.015(2)
O(4)	8e	0	0.5	0.0901(3)	1.00	0.001(2)
tetragonal phase		$\text{La}_3\text{Ni}_{1.6}\text{Al}_{0.4}\text{O}_{6.98}$				
space group		$I4/mmm$ (No. 139)				
a (Å)		3.83466(6)				
c (Å)		20.4648(5)				
R_{wp} (%)		7.83				
S		2.08				
atom	site	x	y	z	occ.	U_{iso}
La(1)	4e	0	0	0.3184(2)	1.00	0.009(1)
La(2)	2b	0	0	0.5	1.00	0.009(1)
Ni/Al	4e	0	0	0.0960(2)	0.80/0.20	0.010(1)
O(1)	2a	0	0	0	0.98(3)	0.041(4)
O(2)	4e	0	0	0.2022(3)	1.00	0.025(1)
O(3)	8g	0	0.5	0.0950(2)	1.00	0.017(1)

as-prepared and post-annealed samples, consistent with the increase of oxygen content. Finally, the c/a_p value increases a little with post annealing, in sharp contrast with the very low value of the β phase in the post-annealed $\text{La}_3\text{Ni}_2\text{O}_7$. The realization of the tetragonal phase at ambient pressure here can be basically understood in terms of the concept of Goldschmidt tolerance factor τ . First, τ is increased by the Al doping because of the difference in the ionic radii of $\text{Ni}^{2.5+}$ and Al^{3+} . Second, τ is further increased by the increase of oxygen occupancy at the O1 site. Thus, the Al doping and oxygenation have a synergistic effect on τ , which makes the tetragonal phase finally stabilized.

Electrical resistivity measurements at ambient pressure on $\text{La}_3\text{Ni}_{2-x}\text{Al}_x\text{O}_{7-\delta}$ demonstrate absence of superconductivity in all samples, as shown in Figure 3. One sees that the resistivity increases rapidly with Al doping, and the Al-doped samples show semiconducting or insulating behaviors. The result suggests strong carrier localization induced by Al-doping disorder. The low-temperature resistivity basically follows variable-range hopping (VRH) formula $\rho(T) = \rho_0 \exp(T_0/T)^{1/D}$, where D refers to the dimension in the electron hopping [Figure S4 in SI] [53]. The two-dimensional

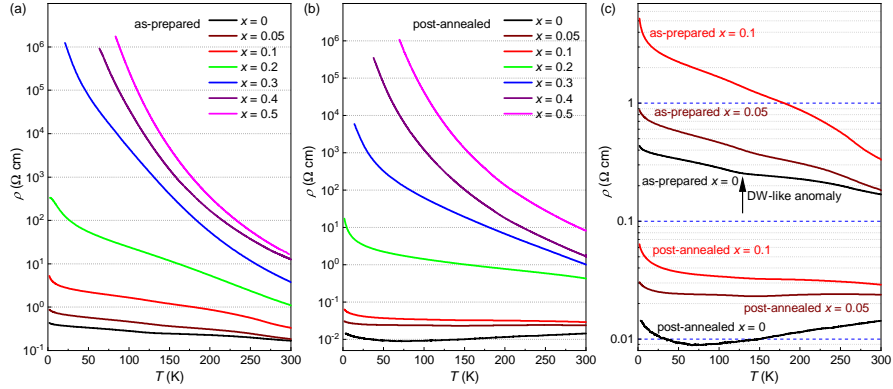


Fig. 3 Temperature dependence of electrical resistivity of the as-prepared (a) and post-annealed (b) samples of $\text{La}_3\text{Ni}_{2-x}\text{Al}_x\text{O}_{7-\delta}$. The effect of post annealing is highlighted in panel (c) for $x = 0, 0.05$ and 0.1 .

VRH better fits the data, suggesting that disorder effects are confined to the NiO_2 planes. One also note that the resistivity of the post-annealed samples is systematically reduced, which inversely implies that the oxygen vacancy in the as-prepared samples also contributes the carrier localization [20]. For the as-prepared undoped sample, an anomaly at ~ 125 K can be detected, similar to the earlier reports in $\text{La}_3\text{Ni}_2\text{O}_{6.92}$ polycrystalline sample [18, 20]. The anomaly has been recently identified as the density-wave (DW) transition [1, 54]. This DW-like transition is smeared out at $x = 0.1$, and becomes indiscernible for $x \geq 0.2$. The result indicates that the Al doping destroys the DW order either [39]. For the post-annealed samples, no signature of DW transition is present even in the undoped parent compound, primarily due to phase transformation into the β phase, similar to the very recent report [41].

Figure 4 shows the magnetic susceptibility data measured under a magnetic field of $\mu_0 H = 0.1$ T for all samples of $\text{La}_3\text{Ni}_{2-x}\text{Al}_x\text{O}_{7-\delta}$. The undoped samples exhibit relatively low values of magnetic susceptibility (~ 0.001 emu/mol) with a weak temperature dependence. At high temperatures above ~ 100 K, the susceptibility decreases with decreasing temperature, suggesting existence of antiferromagnetic correlations. Upon Al doping, the magnetic susceptibility increases systematically, and the high-temperature $\chi(T)$ data for $x > 0.1$ basically follows the extended Curie-Weiss formula, $\chi = \chi_0 + C/(T + \theta_W)$, where χ_0 , C , and θ_W represent the temperature-independent term, the Curie constant, and the paramagnetic Curie-Weiss temperature, respectively. The data fitting in the temperature range of 150-300 K [Figures 4(b) and 4(d)] yields the three parameters, which are presented in Table S2 in the SI. The χ_0 values are all around 0.001 emu/mol, basically identical to the χ value of the undoped samples. The Curie constant increases progressively with Al doping, and the derived effective magnetic moments (μ_{eff}) increase from 0.48 ($x = 0.2$) to 1.01 ($x = 0.5$) μ_B/Ni for the as-prepared samples. A similar trend is also observed for the post-annealed samples with $x > 0.2$. At low temperatures, one sees that the FC and ZFC data bifurcate for Al-doped samples, suggesting freezing of localized spins. Evidenced of the spin freezing is also given by the magnetic hysteresis at the lowest temperature measured (Figure

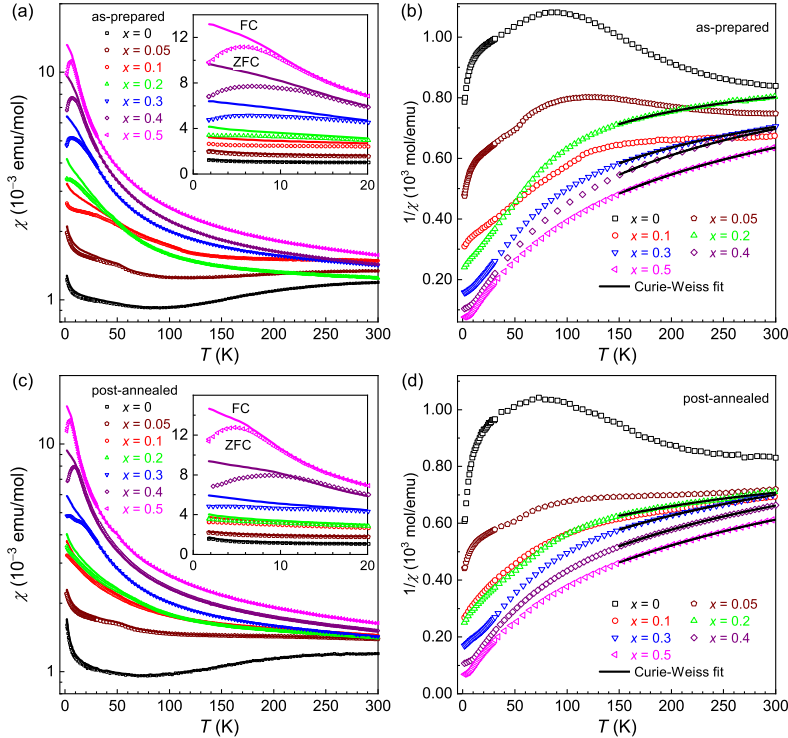


Fig. 4 Magnetic susceptibility data for the as-prepared (a,b) and post-annealed (c,d) samples of $\text{La}_3\text{Ni}_{2-x}\text{Al}_x\text{O}_{7-\delta}$. In panels (a) and (c), a logarithmic scale is used to distinctly show the lower-value data. FC and ZFC denote field cooling and zero field cooling, respectively.

S5 in the SI). While oxygen annealing increases the absolute susceptibility values very slightly, the magnetic parameters remain nearly unchanged, demonstrating that Al doping rather than oxygen content dominates the magnetic modifications, mirroring observations in Zn-doped cuprates where nonmagnetic impurities induce moments independent of oxygen-content variations [55, 56].

To investigate the potential pressure-induced superconductivity in Al-doped $\text{La}_3\text{Ni}_2\text{O}_{7-\delta}$, we performed temperature-dependent resistance measurements on the undoped sample $\text{La}_3\text{Ni}_2\text{O}_{7-\delta}$ (pure orthorhombic phase after oxygen-annealing at 400°C) and post-annealed samples ($x = 0.05, 0.1,$ and 0.4) under pressures. As shown in Figure 5(a), the undoped sample displays a superconducting transition at $T_c \approx 80$ K, consistent with previous reports [1–3]. The observed broad transition might arise from sample inhomogeneity and/or weak links between crystalline grains. The $x = 0.05$ sample [Figure 5(b)] maintains semiconducting behavior at low pressures but shows a pronounced resistance drop below 12 K at 24.8 GPa. This drop is probably associated with the emergence of a superconducting transition. In contrast, the $x = 0.1$ sample [Figure 5(c)] and tetragonal phase $x = 0.4$ sample [Figure S7 in SI] keep semiconducting/insulating behavior within measured pressure range and have large resistance values even over 20 GPa, implying stronger carrier localization with

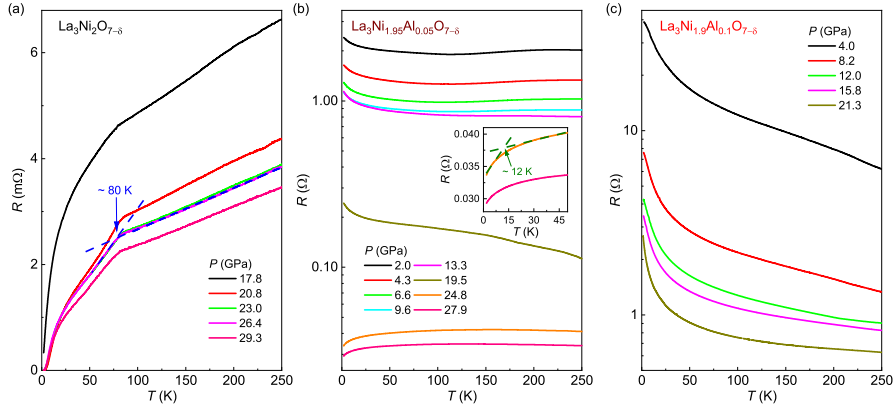


Fig. 5 Temperature dependence of resistance under pressures for $\text{La}_3\text{Ni}_2\text{O}_{7-\delta}$ (a), $\text{La}_3\text{Ni}_{1.95}\text{Al}_{0.05}\text{O}_{7-\delta}$ (b) and $\text{La}_3\text{Ni}_{1.9}\text{Al}_{0.1}\text{O}_{7-\delta}$ (c). T_c is determined as the interception between two linear extrapolations below and above the superconducting transition. The inset in panel (b) shows an enlargement of the $R(T)$ for $x = 0.05$ sample at 24.8 and 27.9 GPa below 50 K. phases with orthorhombic ones.

increased Al doping. Furthermore, the orthorhombic $x = 0.05$ sample annealed at the lower temperature of 400 °C remains insulating at 24.7 GPa [Figure S8 in SI], likely due to insufficient oxygen content. These results indicate that a low Al substitution at $\sim 2.5\%$ can effectively destroy superconductivity in this system.

Figure 6 plots the ambient-pressure electrical resistivity at 100 K, $\rho_{100\text{K}}$, and the effective magnetic moments derived above as functions of Al content. The $\rho_{100\text{K}}$ value increases almost exponentially with the Al doping, independent of the oxygenation by post annealing (although the resistivities are nearly two orders of magnitude reduced) and the crystal-structure transformation. The result indicates that the Al dopant dominates the carrier localization. Remarkably, such a localization can be weakened by the A-site chemical substitution, as suggested from a latest report [57]. Note that free local moments are absent in the undoped samples, while the Al-doped samples do carry local magnetic moments. The effective magnetic moments originate from Al doping, similar to the case in cuprates [55, 56, 58]. As shown in Figure 6, the calculated values of effective moments, assuming that each Al atom induces a spin-1/2 localized moment, align closely with the experimental ones. This supports the interpretation that Al^{3+} locally disrupts the magnetic order in the NiO_2 planes. The inset of Figure 6 shows that T_c decreases rapidly as Al doping increases in $\text{La}_3\text{Ni}_{2-x}\text{Al}_x\text{O}_{7-\delta}$, similar to the effect of Zn doping in $\text{YBa}_2\text{Cu}_{3-x}\text{Zn}_x\text{O}_{7-\delta}$ [59]. Given that nonmagnetic scattering breaks Cooper pairs and significantly suppresses T_c in unconventional superconductors [60, 61], the dramatic reduction of T_c by a small amount of nonmagnetic impurity provides strong evidence for unconventional superconductivity in $\text{La}_3\text{Ni}_2\text{O}_{7-\delta}$.

In summary, we have successfully realized the tetragonal phase of bilayer nickelate at ambient pressure by Al doping together with post annealing in oxygen atmosphere ($P_{\text{O}_2} \approx 10$ MPa). The stabilization of the tetragonal structure can be basically understood with the concept of Goldschmidt tolerance factor. We also found that the post-annealed undoped sample partially transforms into another tetragonal phase—the

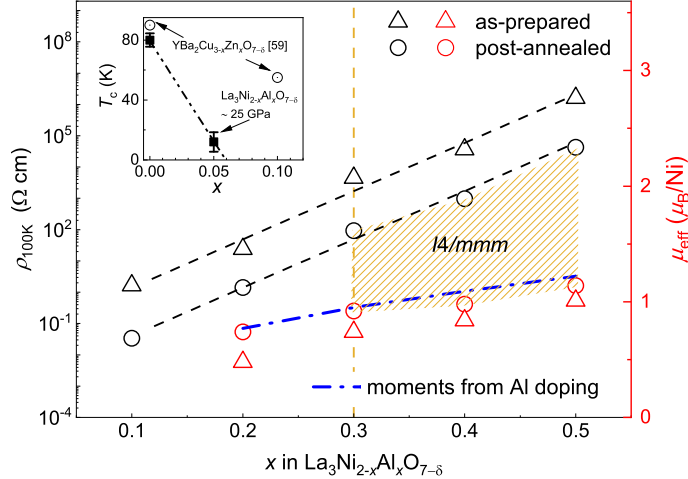


Fig. 6 Electrical resistivity at 100 K (left axis) and effective magnetic moments (right axis) as functions of Al doping in $\text{La}_3\text{Ni}_{2-x}\text{Al}_x\text{O}_{7-\delta}$. The black dashed lines are guides to the eye, and the dash-dotted line represents the expected effective moments induced by Al doping. The yellow trapezoidal area merely indicates the experimental parameter range ($0.3 \leq x \leq 0.5$) where the $I4/mmm$ tetragonal phase was observed in this study. The inset demonstrates the relationship between T_c and doping content in $\text{La}_3\text{Ni}_{2-x}\text{Al}_x\text{O}_{7-\delta}$ at ~ 25 GPa and $\text{YBa}_2\text{Cu}_{3-x}\text{Zn}_x\text{O}_{7-\delta}$ at ambient pressure [59].

β phase. This β phase is significantly different from the Al-doped tetragonal one in the light of the axial ratio c/a_p . Note that the c/a_p value of the latter is similar to that of the superconducting bilayer nickelate under high pressures. Thus, our work provides an initial step towards the ultimate realization of bulk HTSC at ambient pressure.

The aluminum doping also serves as a probe in the system, which significantly alters the physical properties. Even at a low doping level, the system evolves from a bad metal to a semiconductor, and significantly suppresses pressure-induced superconductivity. The resistivity increases almost exponentially with the Al doping, indicating that the Al doping induces strong disorder. Notably, the Al doping also induces local magnetic moments, a phenomenon reminiscent of nonmagnetic doping effect in cuprate superconductors. It would be worthwhile to dope with an element in proximity to nickel to lower the localization effect in the future.

3 METHODS

Polycrystalline samples of $\text{La}_3\text{Ni}_{2-x}\text{Al}_x\text{O}_{7-\delta}$ ($0 \leq x \leq 0.6$) were synthesized by solid-state reactions using a sol-gel produced precursor. [18, 24] Stoichiometric mixture of the source materials, $\text{La}(\text{NO}_3)_3 \cdot 6\text{H}_2\text{O}$ (99.9% Aladdin), $\text{Ni}(\text{NO}_3)_2 \cdot 6\text{H}_2\text{O}$ (99.99% Aladdin), and $\text{Al}(\text{NO}_3)_3 \cdot 9\text{H}_2\text{O}$ (99.99% Aladdin), were dissolved in the glycol and deionized water with addition of appropriate amount of citric acid. The mixed solution was continuously stirred in a water bath (90 °C) for 4 h, and homogeneous green gel resulted. The gel was slowly heated to 500 °C in air, and then further heated to 800 °C, holding for 10 h to eliminate organic components. The resulted precursor was

ground and pressed into pellets, and the pellets were sintered in air at 1080-1150 °C for 50 h, which produces single-phase samples of $\text{La}_3\text{Ni}_{2-x}\text{Al}_x\text{O}_{7-\delta}$. In order to obtain the tetragonal phase, the as-prepared samples were post annealed at 500 °C for 30 h in 10 MPa oxygen atmosphere.

Powder XRD data were collected on a PANalytical diffractometer (Empyrean Series 2) with $\text{Cu-}K_{\alpha 1}$ radiation. TGA measurements were accomplished in HQT-3, using a 10% H_2/Ar gas flow of 3 mL/min with a 20 °C/min rate up to 740 °C. The NPD measurements were carried out on the high-resolution neutron diffractometer at the Key Laboratory of Neutron Physics, Institute of Nuclear Physics and Chemistry, China Academy of Engineering Physics. The wavelength of the neutron was $\lambda = 1.8846 \text{ \AA}$. The crystal structure was refined by Rietveld analysis using the GSAS-II package [62]. The chemical composition was determined using EDX spectroscopy on a scanning electron microscope (Hitachi S-3700N) equipped with Oxford Instruments X-Max spectrometer. Electrical resistivity was measured on a Quantum Design Physical Property Measurement System (PPMS-9) using standard four-electrodes method. The magnetic properties were measured on a Quantum Design Magnetic Property Measurement System (MPMS3). Resistance measurements under pressures were performed in a diamond anvil cell (DAC) using Daphne oil 7373 as the pressure-transmitting medium [3], pressure is determined at room temperature using the ruby fluorescence method [63].

Data availability. The data that support the findings of this study are available from the corresponding author upon reasonable request.

Acknowledgements. We thank Wu-Zhang Yang and Zhi Ren for their help in the electrical resistivity measurement. This work was supported by the National Natural Science Foundation of China (12494593, 12494592 and 12034017), the National Key Research and Development Program of China (2022YFA1403202, 2022YFA1402200 and 2023YFA1406101) and the CAS Superconducting Research Project under Grant No. [SCZX-0101].

Competing interests. The authors declare no competing interests.

Author contributions. G.H.C designed the project; J.Y.L. synthesized the materials and measured transport and magnetic properties; K.X.Y. and Y.N.Z. conducted the high-pressure resistance measurements; H.L. and B.J.L. measured the NPD data; J.X.L. measured the TGA data; J.Y.L. and Y.Q.L. carried out the structural characterizations (XRD and NPD) and performed data analysis with the support of G.H.C, H.Q.Y., K.X.Y., X.Y.Z., J.X.L. and Y.N.Z.; G.H.C., J.Y.L. and Y.Q.L. wrote the paper with inputs from all coauthors.

Appendix A Supplemental Information: Stabilization of Tetragonal Phase and Aluminum-Doping Effect in a Bilayer Nickelate

Contents

- Figure S1. Energy dispersive X-ray (EDX) spectroscopy for $\text{La}_3\text{Ni}_{1.6}\text{Al}_{0.4}\text{O}_{7-\delta}$.
- Figure S2. XRD Rietveld refinements for post-annealed $\text{La}_3\text{Ni}_2\text{O}_{7-\delta}$ and $\text{La}_3\text{Ni}_{1.9}\text{Al}_{0.1}\text{O}_{7-\delta}$.
- Figure S3. Thermogravimetric curves for representative as-prepared and post-annealed $\text{La}_3\text{Ni}_{2-x}\text{Al}_x\text{O}_{7-\delta}$.
- Figure S4. XRD Rietveld refinements for as-prepared and post-annealed $\text{La}_3\text{Ni}_{1.6}\text{Al}_{0.4}\text{O}_{7-\delta}$.
- Figure S5. The linear fits of $\ln\rho$ to $T^{-1/3}$ and $T^{-1/4}$ for $\text{La}_3\text{Ni}_{2-x}\text{Al}_x\text{O}_{7-\delta}$ samples.
- Figure S6. Isothermal magnetization for $\text{La}_3\text{Ni}_{2-x}\text{Al}_x\text{O}_{7-\delta}$ samples.
- Figure S7. Temperature dependence of resistance under pressures for post-annealed $\text{La}_3\text{Ni}_{2-x}\text{Al}_x\text{O}_{7-\delta}$.
- Figure S8. Temperature dependence of resistance under pressures for $\text{La}_3\text{Ni}_{1.95}\text{Al}_{0.05}\text{O}_{7-\delta}$ annealed at 400 °C in oxygen.
- Table S1. Crystallographic data of $\text{La}_3\text{Ni}_{1.6}\text{Al}_{0.4}\text{O}_{7-\delta}$ from XRD.
- Table S2. The Curie-Weiss fit parameters for $\text{La}_3\text{Ni}_{2-x}\text{Al}_x\text{O}_{7-\delta}$ ($0.2 \leq x \leq 0.5$).

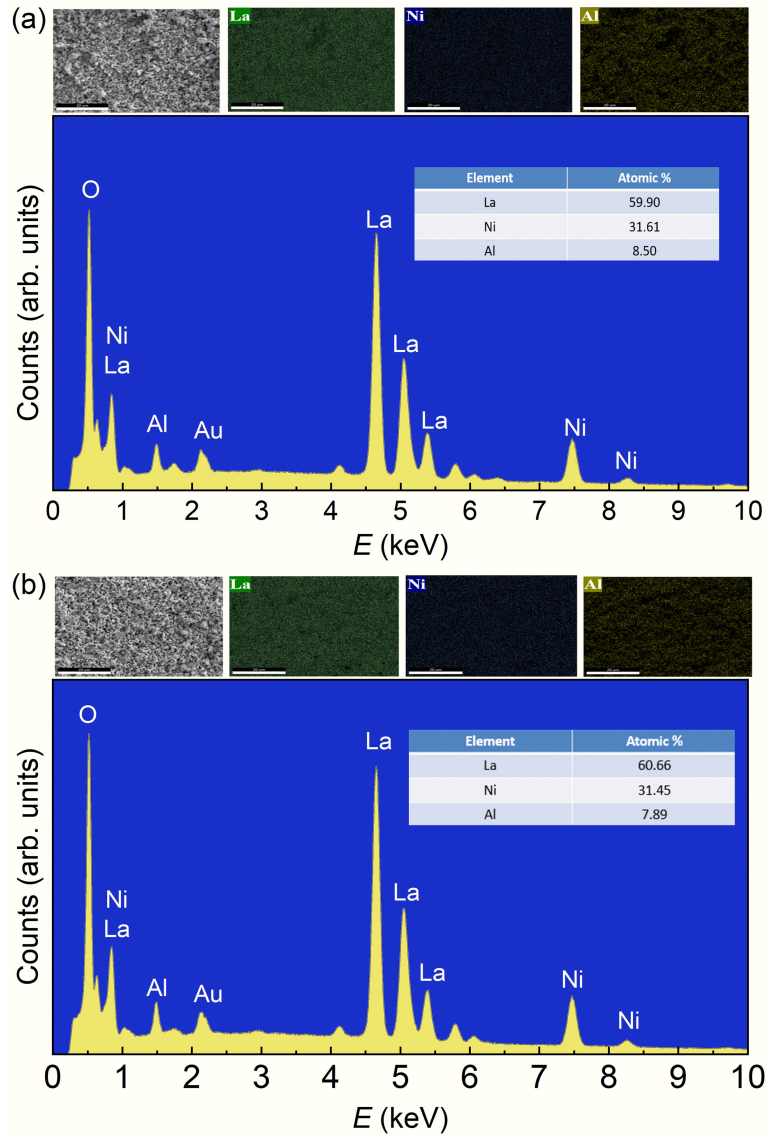


Fig. S1 Verification of the chemical compositions of the as-prepared (a) and post-annealed (b) samples of $\text{La}_3\text{Ni}_{1.6}\text{Al}_{0.4}\text{O}_{7-\delta}$ by energy dispersive X-ray spectroscopy. The atomic ratios of cations are La: Ni: Al = 3: 1.58: 0.43 and 3: 1.56: 0.39, respectively, for the as-prepared and post-annealed samples. The oxygen content is not analyzed here because of the inherent large measurement uncertainty. Note that the surface of the sample was sprayed with gold, in order to avoid the accumulation of electric charge.

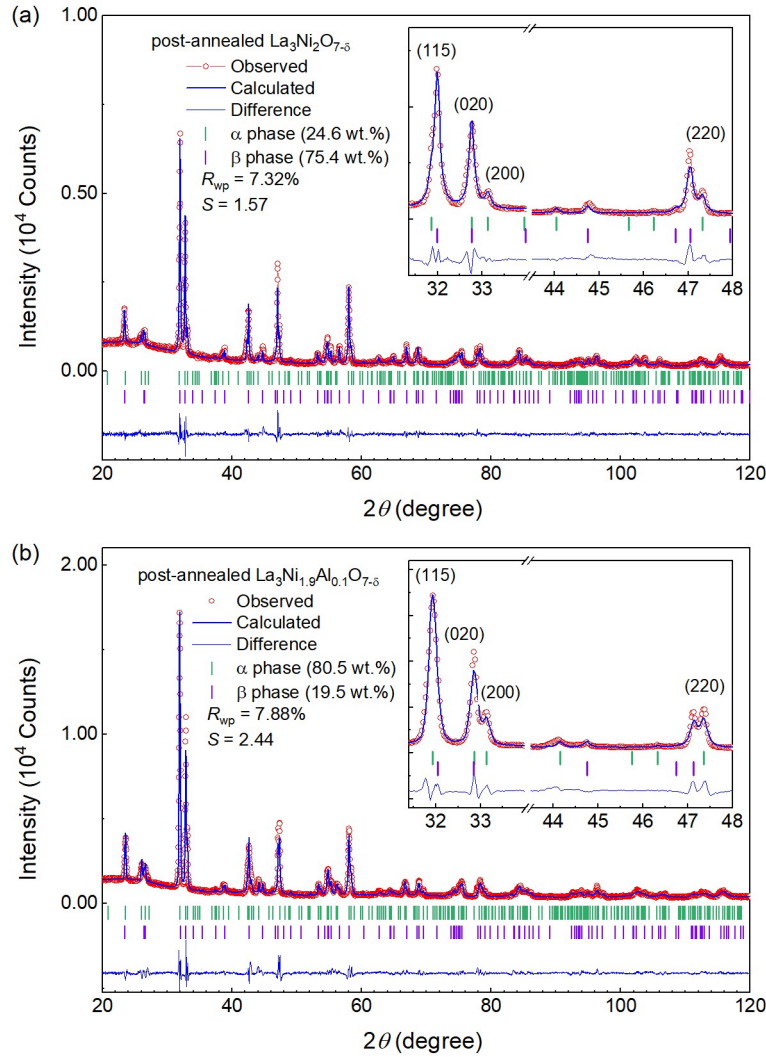


Fig. S2 Two-phase Rietveld refinement profiles based on powder X-ray diffraction data for post-annealed $\text{La}_3\text{Ni}_2\text{O}_{7-\delta}$ (a) and $\text{La}_3\text{Ni}_{1.9}\text{Al}_{0.1}\text{O}_{7-\delta}$ (b). The α phase has the normal orthorhombic bilayer structure ($Amam$), while the β phase is modelled with $\text{K}_3\text{Ni}_2\text{F}_7$ -type structure ($I4/mmm$). The insets show some of the main reflections. For non-doped $\text{La}_3\text{Ni}_2\text{O}_{7-\delta}$, the refined lattice parameters are, $a = 5.3931(4)$ Å, $b = 5.4509(6)$ Å, $c = 20.5167(15)$ Å for the $\text{La}_3\text{Ni}_2\text{O}_{7-\delta}$ α phase (24.6 wt.%); and $a = 3.8552(1)$ Å, $c = 20.2120(8)$ Å for the β phase (75.4 wt.%). In the case of the Al-doped $\text{La}_3\text{Ni}_{1.9}\text{Al}_{0.1}\text{O}_{7-\delta}$, the cell parameters are $a = 5.4049(2)$ Å, $b = 5.4487(2)$ Å, $c = 20.5009(10)$ Å for the α phase (80.5 wt.%); and $a = 3.8543(2)$ Å, $c = 20.2418(17)$ Å for the β phase (19.5 wt.%).

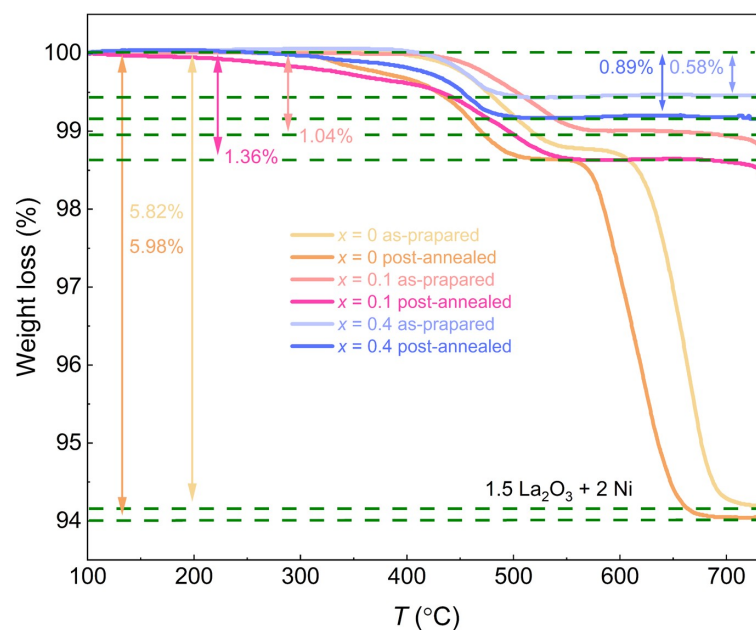


Fig. S3 Thermogravimetric curves for as-prepared and post-annealed $\text{La}_3\text{Ni}_{2-x}\text{Al}_x\text{O}_{7-\delta}$ ($x = 0, 0.1, 0.4$). The oxygen stoichiometry was determined as $\text{La}_3\text{Ni}_2\text{O}_{6.84}$ for the as-prepared phase and $\text{La}_3\text{Ni}_2\text{O}_{6.91}$ for the post-annealed phase, with the slight deviation from stoichiometry attributed to the presence of about 5 wt.% La_2NiO_4 in the samples used for TGA. For $x = 0.1$ samples, analysis of the weight-loss plateaus corresponding to $\text{La}_3\text{Ni}_{1.9}\text{Al}_{0.1}\text{O}_{6.45}$ yields oxygen contents of about 6.87 (as-prepared) and 7.00 (post-annealed).

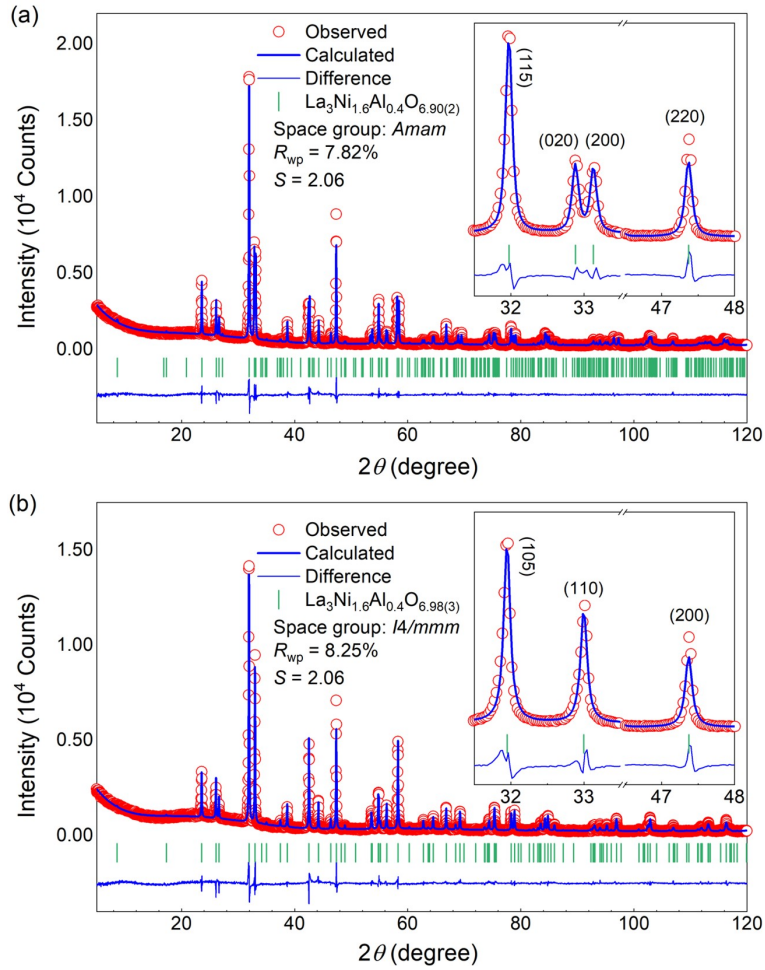


Fig. S4 Rietveld refinement profiles based on powder X-ray diffraction data for as-prepared $\text{La}_3\text{Ni}_{1.6}\text{Al}_{0.4}\text{O}_{6.90(2)}$ (a) and post-annealed $\text{La}_3\text{Ni}_{1.6}\text{Al}_{0.4}\text{O}_{6.98(3)}$ (b). The obtained lattice parameters are, $a = 5.40466(7)$ Å, $b = 5.44409(7)$ Å, $c = 20.4439(3)$ Å for the as-prepared $\text{La}_3\text{Ni}_{1.6}\text{Al}_{0.4}\text{O}_{6.90(2)}$; and $a = 3.83438(4)$ Å, $c = 20.4620(4)$ Å for the post-annealed $\text{La}_3\text{Ni}_{1.6}\text{Al}_{0.4}\text{O}_{6.98(3)}$.

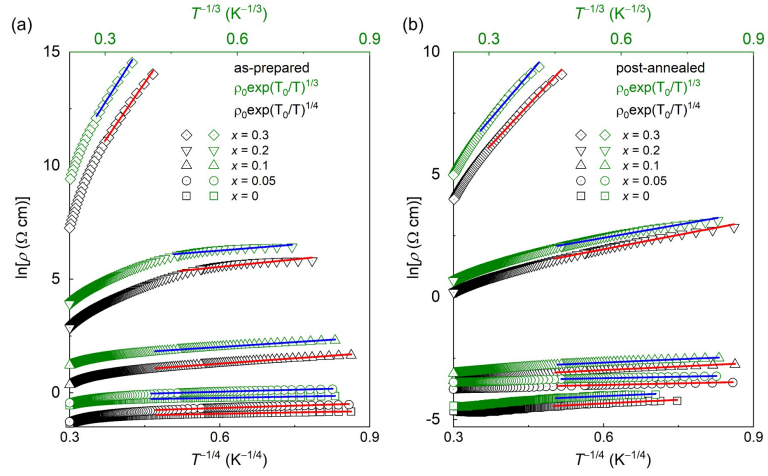


Fig. S5 The linear fits of $\ln\rho$ to $T^{-1/3}$ (blue lines) and $T^{-1/4}$ (red lines) for the as-prepared (a) and post-annealed (b) samples of $\text{La}_3\text{Ni}_{2-x}\text{Al}_x\text{O}_{7-\delta}$ ($x \leq 0.3$) in the low temperature regime.

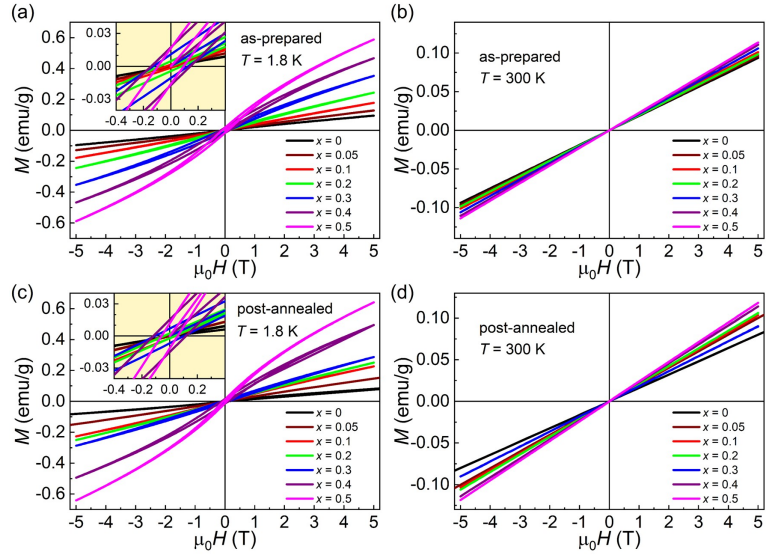


Fig. S6 Isothermal magnetization for the as-prepared (a, b) and post-annealed (c, d) samples of $\text{La}_3\text{Ni}_{2-x}\text{Al}_x\text{O}_{7-\delta}$ at 1.8 K and 300 K.

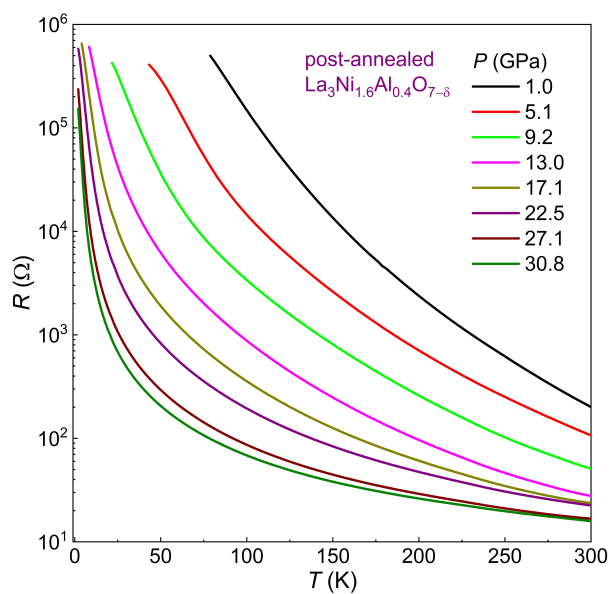


Fig. S7 Temperature dependence of resistance under pressures for post-annealed $\text{La}_3\text{Ni}_{1.6}\text{Al}_{0.4}\text{O}_{7-\delta}$.

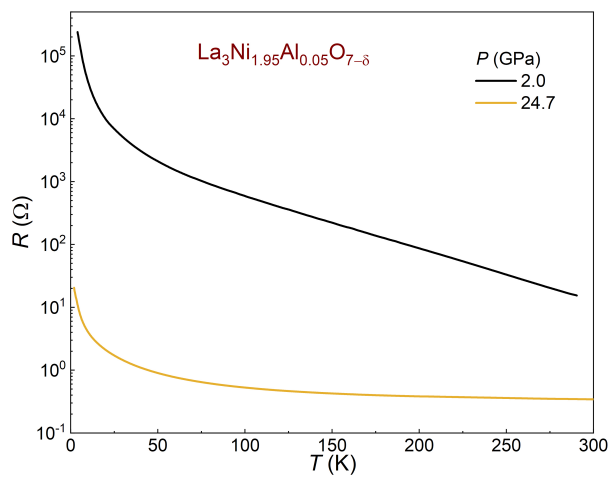


Fig. S8 Temperature dependence of resistance under pressures for the orthorhombic phase of $\text{La}_3\text{Ni}_{1.95}\text{Al}_{0.05}\text{O}_{7-\delta}$ annealed in 10 MPa oxygen at 400 °C for 30h.

Table S1 Crystallographic data of the as-prepared (*Amam* phase) and post-annealed (*I4/mmm* phase) $\text{La}_3\text{Ni}_{1.6}\text{Al}_{0.4}\text{O}_{7-\delta}$ from X-ray powder diffractions.

$\text{La}_3\text{Ni}_{1.6}\text{Al}_{0.4}\text{O}_{6.90}$			<i>Amam</i> (No.63)		
atom	x	y	z	occ.	U_{iso}
La(1)	0.25	0.249(2)	0.5	1.00	0.004(1)
La(2)	0.25	0.242(1)	0.3195(1)	1.00	0.004(1)
Ni/Al	0.25	0.248(4)	0.0971(3)	0.80/0.20	0.007(2)
O(1)	0.25	0.288(14)	0	0.90(2)	0.013(13)
O(2)	0.25	0.311(5)	0.1996(10)	1.00	0.015(8)
O(3)	0.5	0	0.105(2)	1.00	0.001(11)
O(4)	0	0.5	0.091(2)	1.00	0.015(8)
$\text{La}_3\text{Ni}_{1.6}\text{Al}_{0.4}\text{O}_{6.98}$			<i>I4/mmm</i> (No.139)		
atom	x	y	z	occ.	U_{iso}
La(1)	0	0	0.3198(2)	1.00	0.004(1)
La(2)	0	0	0.5	1.00	0.004(1)
Ni/Al	0	0	0.0977(4)	0.80/0.20	0.016(2)
O(1)	0	0	0	0.98(3)	0.012(11)
O(2)	0	0	0.191(2)	1.00	0.051(13)
O(3)	0	0.5	0.0965(10)	1.00	0.033(7)

Table S2 The Curie-Weiss fit parameters for $\text{La}_3\text{Ni}_{2-x}\text{Al}_x\text{O}_{7-\delta}$ ($0.2 \leq x \leq 0.5$).

doping content (as-prepared)	0.2	0.3	0.4	0.5
χ_0 (emu mol ⁻¹)	0.00011	0.0011	0.0010	0.0010
θ_W (K)	8.50	30.96	17.78	27.02
C (emu K mol ⁻¹ fu ⁻¹)	0.051	0.12	0.14	0.19
μ_{eff} (μ_B/Ni)	0.48	0.74	0.84	1.01
doping content (post-annealed)	0.2	0.3	0.4	0.5
χ_0 (emu mol ⁻¹)	0.00096	0.00095	0.00095	0.00092
θ_W (K)	100	84.68	50.72	49.98
C (emu K mol ⁻¹ fu ⁻¹)	0.12	0.18	0.19	0.24
μ_{eff} (μ_B/Ni)	0.74	0.92	0.98	1.14

References

- [1] Sun, H., *et al.*: Signatures of superconductivity near 80 K in a nickelate under high pressure. *Nature* **621**(621), 493–498 (2023)
- [2] Wang, G., *et al.*: Pressure-induced superconductivity in polycrystalline $\text{La}_3\text{Ni}_2\text{O}_{7-\delta}$. *Phys. Rev. X* **14**, 011040 (2024)
- [3] Zhang, Y., *et al.*: High-temperature superconductivity with zero resistance and strange-metal behaviour in $\text{La}_3\text{Ni}_2\text{O}_{7-\delta}$. *Nat. Phys.* **20**(8), 1269–1273 (2024)
- [4] Li, D., *et al.*: Superconductivity in an infinite-layer nickelate. *Nature* **572**(7771), 624–627 (2019)
- [5] Shen, Y., Qin, M., Zhang, G.-M.: Effective bi-layer model hamiltonian and density-matrix renormalization group study for the High- T_c superconductivity in $\text{La}_3\text{Ni}_2\text{O}_7$ under high pressure. *Chin. Phys. Lett.* **40**(12) (2023)
- [6] Lechermann, F., *et al.*: Electronic correlations and superconducting instability in $\text{La}_3\text{Ni}_2\text{O}_7$ under high pressure. *Phys. Rev. B* **108**, 201121 (2023)
- [7] Zhang, Y., *et al.*: Electronic structure, dimer physics, orbital-selective behavior, and magnetic tendencies in the bilayer nickelate superconductor $\text{La}_3\text{Ni}_2\text{O}_7$ under pressure. *Phys. Rev. B* **108**, 180510 (2023)
- [8] Yang, Y., Zhang, G., Zhang, F.: Interlayer valence bonds and two-component theory for high- T_c superconductivity of $\text{La}_3\text{Ni}_2\text{O}_7$ under pressure. *Phys. Rev. B* **108**, 201108 (2023)
- [9] Liu, Y., *et al.*: s^\pm -wave pairing and the destructive role of apical-oxygen deficiencies in $\text{La}_3\text{Ni}_2\text{O}_7$ under pressure. *Phys. Rev. Lett.* **131**, 236002 (2023)
- [10] Sakakibara, H., Kitamine, N., Ochi, M., Kuroki, K.: Possible high T_c superconductivity in $\text{La}_3\text{Ni}_2\text{O}_7$ under high pressure through manifestation of a nearly half-filled bilayer hubbard model. *Phys. Rev. Lett.* **132**, 106002 (2024)
- [11] Geisler, B., Hamlin, J.J., Stewart, G.R., Hennig, R.G., Hirschfeld, P.J.: Structural transitions, octahedral rotations, and electronic properties of $A_3\text{Ni}_2\text{O}_7$ rare-earth nickelates under high pressure. *npj Quantum Mater.* **9**(9), 38 (2024)
- [12] Geisler, B., *et al.*: Optical properties and electronic correlations in $\text{La}_3\text{Ni}_2\text{O}_7$ bilayer nickelates under high pressure. *npj Quantum Mater.* **9**(9), 89 (2024)
- [13] Lu, C., Pan, Z., Yang, F., Wu, C.: Interlayer-coupling-driven high-temperature superconductivity in $\text{La}_3\text{Ni}_2\text{O}_7$ under pressure. *Phys. Rev. Lett.* **132**, 146002 (2024)
- [14] Qu, X., *et al.*: Bilayer $t-J-J_\perp$ model and magnetically mediated pairing in the

- pressurized nickelate $\text{La}_3\text{Ni}_2\text{O}_7$. *Phys. Rev. Lett.* **132**, 036502 (2024)
- [15] Deng, L., *et al.*: Creation, stabilization, and investigation at ambient pressure of pressure-induced superconductivity in $\text{Bi}_{0.5}\text{Sb}_{1.5}\text{Te}_3$. *PNAS* **122**(6), 2423102122 (2025)
- [16] Xu, M., *et al.*: Pressure-dependent “insulator–metal–insulator” behavior in Sr-doped $\text{La}_3\text{Ni}_2\text{O}_7$. *Advanced Electronic Materials* **10**(9), 2400078 (2024)
- [17] Drennan, J., Tavares, C.P., Steele, B.C.H.: An electron microscope investigation of phases in the system La-Ni-O. *Mater. Res. Bull.* **17**(5), 621–626 (1982)
- [18] Zhang, Z., Greenblatt, M., Goodenough, J.: Synthesis, structure, and properties of the layered perovskite $\text{La}_3\text{Ni}_2\text{O}_{7-\delta}$. *J. Solid State Chem.* **108**(2), 402–409 (1994)
- [19] Sreedhar, K., *et al.*: Low-temperature electronic properties of the $\text{La}_{n+1}\text{Ni}_n\text{O}_{3n+1}$ ($n = 2, 3$, and ∞) system: Evidence for a crossover from fluctuating-valence to fermi-liquid-like behavior. *J. Solid State Chem.* **110**(2), 208–215 (1994)
- [20] Taniguchi, S., *et al.*: Transport, magnetic and thermal properties of $\text{La}_3\text{Ni}_2\text{O}_{7-\delta}$. *J. Phys. Soc. Jpn.* **64**(5), 1644–1650 (1995)
- [21] Ling, C., Argyriou, D., Wu, G., J., N.: Neutron diffraction study of $\text{La}_3\text{Ni}_2\text{O}_7$: Structural relationships among $n = 1, 2$, and 3 phases $\text{La}_{n+1}\text{Ni}_n\text{O}_{3n+1}$. *J. Solid State Chem.* **152**(2), 517–525 (2000)
- [22] Wang, L., *et al.*: Structure responsible for the superconducting state in $\text{La}_3\text{Ni}_2\text{O}_7$ at high-pressure and low-temperature conditions. *J. Am. Chem. Soc.* **146**(11), 7506–7514 (2024)
- [23] Li, J., *et al.*: Identification of superconductivity in bilayer nickelate $\text{La}_3\text{Ni}_2\text{O}_7$ under high pressure up to 100 GPa. *Natl. Sci. Rev.*, 220 (2025)
- [24] Wang, N., *et al.*: Bulk high-temperature superconductivity in pressurized tetragonal $\text{La}_2\text{PrNi}_2\text{O}_7$. *Nature* **634**, 579–584 (2024)
- [25] Zhu, Y., *et al.*: Superconductivity in pressurized trilayer $\text{La}_4\text{Ni}_3\text{O}_{10-\delta}$ single crystals. *Nature* **631**, 531–536 (2024)
- [26] Ko, E., *et al.*: Signatures of ambient pressure superconductivity in thin film $\text{La}_3\text{Ni}_2\text{O}_7$. *Nature* **638**, 935–940 (2025)
- [27] Zhou, G., *et al.*: Ambient-pressure superconductivity onset above 40 K in $(\text{La,Pr})_3\text{Ni}_2\text{O}_7$ films. *Nature* **640**, 641–646 (2025)
- [28] Liu, Y., *et al.*: Superconductivity and normal-state transport in compressively strained $\text{La}_2\text{PrNi}_2\text{O}_7$ thin films. *Nat. Mater.* **24**, 1221–1227 (2025)

- [29] Goldschmidt, V.M.: Die gesetze der krystallochemie. *Naturwissenschaften* **14**, 477–485 (1926)
- [30] Li, Z., *et al.*: Stabilizing perovskite structures by tuning tolerance factor: Formation of formamidinium and cesium lead iodide solid-state alloys. *Chem. Mater.* **28**(1), 284–292 (2016)
- [31] Shannon, R.D.: Revised effective ionic-radii and systematic studies of interatomic distances in halides and chalcogenides. *Acta Crystallogr., Sect. A* **32**, 751–767 (1976)
- [32] Kharlamova, I., *et al.*: Ruddlesden-popper phases $\text{Sr}_3\text{Ni}_{2-x}\text{Al}_x\text{O}_{7-\delta}$ and some doped derivatives: Synthesis, oxygen nonstoichiometry and electrical properties. *Solid State Ion.* **324**, 241–246 (2018)
- [33] Yilmaz, H., *et al.*: Realization of a classical ruddlesden popper type bilayer nickelate in $\text{Sr}_3\text{Ni}_{2-x}\text{Al}_x\text{O}_{7-\delta}$ with unusual Ni^{4+} . *npj Quantum Mater.* **9**, 92–100 (2024)
- [34] Yamane, K., *et al.*: High-pressure synthesis of bilayer nickelate $\text{Sr}_3\text{Ni}_2\text{O}_5\text{Cl}_2$ with a tetragonal crystal structure. *Acta Cryst. C* **81**, 259–263 (2025)
- [35] Rhodes, L.C., Wahl, P.: Structural routes to stabilize superconducting $\text{La}_3\text{Ni}_2\text{O}_7$ at ambient pressure. *Phys. Rev. Mater.* **8**, 044801 (2024)
- [36] Wu, S., *et al.*: $\text{Ac}_3\text{Ni}_2\text{O}_7$ and $\text{La}_2\text{AeNi}_2\text{O}_6\text{F}$ ($\text{Ae} = \text{Sr}, \text{Ba}$): Benchmark Materials for Bilayer Nickelate Superconductivity (2024). <https://arxiv.org/abs/2403.11713>
- [37] Zhang, Z., Greenblatt, M.: Synthesis, structure, and physical-properties of $\text{La}_{3-x}\text{M}_x\text{Ni}_2\text{O}_{7-\delta}$ ($\text{M} = \text{Ca}^{2+}, \text{Sr}^{2+}, \text{Ba}^{2+}, 0 \leq x \leq 0.075$). *J. Solid State Chem.* **111**(1), 141–146 (1994)
- [38] Aggarwal, L., Božović, I.: The quest for high-temperature superconductivity in nickelates under ambient pressure. *Materials* **17**(11) (2024)
- [39] Periyasamy, M., *et al.*: Effect of electron doping on the crystal structure and physical properties of an $n = 3$ Ruddlesden–Popper compound $\text{La}_4\text{Ni}_3\text{O}_{10}$. *ACS Appl. Electron. Mater.* **3**(6), 2671–2684 (2021)
- [40] Zhang, Y., *et al.*: Damage of bilayer structure in $\text{La}_3\text{Ni}_2\text{O}_{7-\delta}$ induced by high pO_2 annealing (2025). <https://arxiv.org/abs/2502.01501>
- [41] Shi, M., *et al.*: Prerequisite of superconductivity: SDW rather than tetragonal structure in double-layer $\text{La}_3\text{Ni}_2\text{O}_{7-x}$. *Nat. Commun.* **16**, 9141 (2025)
- [42] Liu, Q., *et al.*: Emergence of tetragonal phase in oxygen-annealed Co-doped $\text{La}_3\text{Ni}_2\text{O}_{7+\delta}$. *J. Solid State Chem.* **351**, 125528 (2025)

- [43] Ran, G., *et al.*: Is $\text{La}_3\text{Ni}_2\text{O}_{6.5}$ a bulk superconducting nickelate? *ACS Appl. Mater. Interfaces* **16**(49), 66857–66864 (2024)
- [44] Chen, X., *et al.*: Polymorphism in the Ruddlesden–Popper nickelate $\text{La}_3\text{Ni}_2\text{O}_7$: discovery of a hidden phase with distinctive layer stacking. *J. Am. Chem. Soc.* **146**(6), 3640–3645 (2024)
- [45] Wang, H., Chen, L., Rutherford, A., Zhou, H., Xie, W.: Long-range structural order in a hidden phase of Ruddlesden–Popper bilayer nickelate $\text{La}_3\text{Ni}_2\text{O}_7$. *Inorg. Chem.* **63**(11), 5020–5026 (2024)
- [46] Puphal, P., *et al.*: Unconventional crystal structure of the high-pressure superconductor $\text{La}_3\text{Ni}_2\text{O}_7$. *Phys. Rev. Lett.* **133**, 146002 (2024)
- [47] Jiao, K., *et al.*: Enhanced conductivity in Sr doped $\text{La}_3\text{Ni}_2\text{O}_{7-\delta}$ with high-pressure oxygen annealing. *Physica C* **621**, 1354504 (2024)
- [48] Feng, J., *et al.*: Unaltered density wave transition and pressure-induced signature of superconductivity in Nd-doped $\text{La}_3\text{Ni}_2\text{O}_7$. *Phys. Rev. B* **110**, 100507 (2024)
- [49] Wang, G., *et al.*: Chemical versus physical pressure effects on the structure transition of bilayer nickelates. *npj Quantum Mater.* **10**(1), 1 (2025)
- [50] Rodriguez-Carvajal, J., Fernandez-Diaz, M., Martinez, J.: Neutron diffraction study on structural and magnetic properties of La_2NiO_4 . *J. Phys. Condens. Matter* **3**(19), 3215 (1991)
- [51] Aguadero, A., *et al.*: In situ high temperature neutron powder diffraction study of oxygen-rich $\text{La}_2\text{NiO}_{4+\delta}$ in air: correlation with the electrical behaviour. *J. Mater. Chem.* **16**, 3402–3408 (2006)
- [52] Brown, I.D., Altermatt, D.: Bond-valence parameters obtained from a systematic analysis of the Inorganic Crystal Structure Database. *Acta. Crystallogr. B* **41**(4), 244–247 (1985)
- [53] Shklovskii, B.I., Efros, A.L.: *Electronic Properties of Doped Semiconductors* vol. 45. Springer, Berlin (1984)
- [54] Liu, Z., *et al.*: Evidence for charge and spin density waves in single crystals of $\text{La}_3\text{Ni}_2\text{O}_7$ and $\text{La}_3\text{Ni}_2\text{O}_6$. *Sci. China Phys. Mech. Astron.* **66**, 217411 (2023)
- [55] Mahajan, A.V., Alloul, H., Collin, G., Marucco, J.F.: ^{89}Y NMR probe of Zn induced local moments in $\text{YBa}_2(\text{Cu}_{1-y}\text{Zn}_y)_3\text{O}_{6+x}$. *Phys. Rev. Lett.* **72**, 3100–3103 (1994)
- [56] Zagoulaev, S., Monod, P., Jégoudez, J.: Magnetic and transport properties of Zn-doped $\text{YBa}_2\text{Cu}_3\text{O}_7$ in the normal state. *Phys. Rev. B* **52**, 10474–10487 (1995)

- [57] Yilmaz, H., et al.: Semiconducting character in Ruddlesden-Popper bilayer nickelate $\text{Y}_{0.5}\text{Sr}_{2.5}\text{Ni}_{2-x}\text{Al}_x\text{O}_7$ (2025). <https://arxiv.org/html/2503.07861>
- [58] Ishida, K., Kitaoka, Y., Yamazoe, K., Asayama, K., Yamada, Y.: Al NMR probe of local moments induced by an Al impurity in High- T_c cuprate $\text{La}_{1.85}\text{Sr}_{0.15}\text{CuO}_4$. *Phys. Rev. Lett.* **76**, 531–534 (1996)
- [59] Tarascon, J., et al.: Structural and physical properties of the metal (M) substituted $\text{YBa}_2\text{Cu}_{3-x}\text{M}_x\text{O}_7$ perovskite. *Phys. Rev. B* **37**(13), 7458 (1988)
- [60] Anderson, P.W.: Theory of dirty superconductors. *J. Phys. Chem. Solids* **11**(1-2), 26–30 (1959)
- [61] Millis, A., Sachdev, S., Varma, C.: Inelastic scattering and pair breaking in anisotropic and isotropic superconductors. *Phys. Rev. B* **37**(10), 4975 (1988)
- [62] Toby, B.H., Von Dreele, R.B.: GSAS-II: the genesis of a modern open-source all purpose crystallography software package. *J. Appl. Crystallogr.* **46**(2), 544–549 (2013)
- [63] Mao, H., Xu, J., Bell, P.: Calibration of the ruby pressure gauge to 800 kbar under quasi-hydrostatic conditions. *J. Geophys. Res. Solid Earth* **91**(B5), 4673–4676 (1986)